
This copy is for your personal, non-commercial use only.

If you wish to distribute this article to others, you can order high-quality copies for your colleagues, clients, or customers by [clicking here](#).

Permission to republish or repurpose articles or portions of articles can be obtained by following the guidelines [here](#).

The following resources related to this article are available online at www.sciencemag.org (this information is current as of November 25, 2010):

Updated information and services, including high-resolution figures, can be found in the online version of this article at:

<http://www.sciencemag.org/content/330/6008/1227.full.html>

Supporting Online Material can be found at:

<http://www.sciencemag.org/content/suppl/2010/11/22/330.6008.1227.DC1.html>

This article **cites 12 articles**, 2 of which can be accessed free:

<http://www.sciencemag.org/content/330/6008/1227.full.html#ref-list-1>

This article appears in the following **subject collections**:

Materials Science

http://www.sciencemag.org/cgi/collection/mat_sci

(that is, alkanes from C1 to C6 nonphenolic oxygenates and aromatics from phenolic compounds), requires 14 to 15 g of H₂/100 g of carbon in the feed, if the catalyst coking problems are overcome. In comparison, increasing the H/C_{eff} ratio of pyrolysis oil from 0 to 1.4 requires 11.7 g of H₂/100 g of carbon in the feed, reducing the hydrogen requirements as compared to complete hydrodeoxygenation by 20%. Furthermore, during the hydrotreating process, large amounts of undesired methane are produced, which also can substantially increase the hydrogen requirements. Hydrogen required in these processes should preferably be obtained from renewable sources, such as by the reforming of biomass-derived feedstock (14, 40, 41). Alternatively, hydrogen can be obtained from coal gasification or from water splitting driven by carbon-free energy sources, such as solar, nuclear, and wind energy, as suggested by Agrawal *et al.* (42). Zeolite catalysts convert the biomass feedstocks into aromatics and olefins, which can fit easily into the existing infrastructure. Increasing the yield of petrochemical products from biomass therefore requires hydrogen. Thus, there exists an optimum solution for the economical maximum yield of petrochemical feedstocks products that is dictated by the cost of hydrogen. It is expected that future advances in the field of metal and zeolite catalysts, combined with reaction engineering, will allow us to design even more efficient and economical processes to convert biomass resources to renewable chemical industry feedstocks.

References and Notes

- A. J. Ragauskas *et al.*, *Science* **311**, 484 (2006).
- G. W. Huber, S. Iborra, A. Corma, *Chem. Rev.* **106**, 4044 (2006).
- E. L. Kunkes *et al.*, *Science* **322**, 417 (2008).
- D. L. Klass, *Biomass for Renewable Energy, Fuels and Chemicals* (Academic Press, San Diego, CA, 1998).
- S. Czernik, A. V. Bridgwater, *Energy Fuels* **18**, 590 (2004).
- D. Mohan, C. U. Pittman, P. H. Steele, *Energy Fuels* **20**, 848 (2006).
- M. M. Wright, D. E. Dugaard, J. A. Satrio, R. C. Brown, *Fuel* 10.1016/j.fuel.2010.07.029.
- R. P. Anex *et al.*, *Div. Fuel Chem.* **54**, 704 (2009).
- A. Oasmaa, S. Czernik, *Energy Fuels* **13**, 914 (1999).
- D. C. Elliott, *Energy Fuels* **21**, 1792 (2007).
- T. L. Marker *et al.*, *Opportunities for Biorenewables in Petroleum Refineries* (Final Report, DE-FG36-05G015085, UOP, Des Plaines, IL, 2005); www.osti.gov/bridge/servlets/purl/861458-Wv5uum/861458.pdf.
- J. D. Adjaye, N. N. Bakhshi, *Fuel Proc. Tech.* **45**, 161 (1995).
- J. D. Adjaye, N. N. Bakhshi, *Fuel Proc. Tech.* **45**, 185 (1995).
- T. P. Vispute, G. W. Huber, *Green Chem.* **11**, 1433 (2009).
- C. H. Bartholomew, R. J. Farrauto, *Fundamentals of Industrial Catalytic Processes* (Wiley, Hoboken, NJ, 2006).
- T. F. Degnan Jr., M. Smith, C. R. Venkat, *Appl. Catal. A* **221**, 283 (2001).
- C. Perego, P. Ingallina, *Catal. Today* **73**, 3 (2002).
- G. R. Lappin, J. D. Sauer, Eds., *Alpha Olefins Applications Handbook* (Marcel Dekker, New York, NY, 1989).
- H. H. Zsmant, *Organic Building Blocks of the Chemical Industry* (Wiley, New York, 1989).
- N. Y. Chen, T. F. Degnan Jr., L. R. Koenig, *Chemtech* **16**, 506 (1986).
- A. G. Gayubo, A. T. Aguayo, A. Atutxa, R. Aguado, J. Bilbao, *Ind. Eng. Chem. Res.* **43**, 2610 (2004).
- T. R. Carlson, T. P. Vispute, G. W. Huber, *ChemSusChem* **1**, 397 (2008).
- R. Bayerbach, D. Meier, *J. Anal. Appl. Pyrolysis* **85**, 98 (2009).
- T. A. Milne, F. Agblevor, M. Davis, S. Deutch, D. Johnson, in *Developments in Thermal Biomass Conversion*, A. V. Bridgwater, D. G. B. Boocock, Eds. (Blackie Academic and Professional, London, 1997), pp. 409–424.
- J. S. Shabtai, W. W. Zmierzczak, E. Chornet, U.S. Patent 5,959,167 (1999).
- J. S. Shabtai, W. W. Zmierzczak, E. Chornet, U.S. Patent 6,172,272 (2001).
- J. E. Miller, L. Evans, A. Littlewolf, D. E. Trudell, *Fuel* **78**, 1363 (1999).
- C. Zhao, Y. Kou, A. A. Lemonidou, X. B. Li, J. A. Lercher, *Angew. Chem. Int. Ed.* **48**, 3987 (2009).
- S. Crossley, J. Faria, M. Shen, D. E. Resasco, *Science* **327**, 68 (2010).
- C. Zhao, Y. Kou, A. A. Lemonidou, X. B. Li, J. A. Lercher, *Chem. Commun.* **46**, 412 (2010).
- H. Olcay, L. Xu, Y. Xu, G. W. Huber, *ChemCatChem* 10.1002/cctc.201000134 (2010).
- N. Li, G. W. Huber, *J. Catal.* **270**, 48 (2010).
- Materials, methods, and calculations are available as supporting material on *Science* Online.
- G. W. Huber, R. D. Cortright, J. A. Dumesic, *Angew. Chem. Int. Ed.* **43**, 1549 (2004).
- T. R. Carlson, Y. Cheng, J. Jae, G. W. Huber, *Energy Environ. Sci.* 10.1039/C0EE00341G.
- M. Guisnet, N. S. Gnep, F. Alario, *Appl. Catal. A* **89**, 1 (1992).
- V. R. Choudhary, P. Devadas, S. Banerjee, A. K. Kinage, *Microporous Mesoporous Mater.* **47**, 253 (2001).
- C. E. G. Padro, V. Putsche, *Survey of the Economics of Hydrogen Technologies* (report, NREL/TP-570-27079, National Renewable Energy Laboratory, Golden, CO, 1999); <http://www1.eere.energy.gov/hydrogenandfuelcells/pdfs/27079.pdf>.
- National Research Council and National Academy of Engineering, *The Hydrogen Economy: Opportunities, Costs, Barriers, and R&D Needs* (National Academies Press, Washington, DC, 2004).
- R. D. Cortright, R. R. Davda, J. A. Dumesic, *Nature* **418**, 964 (2002).
- G. W. Huber, J. W. Shabaker, J. A. Dumesic, *Science* **300**, 2075 (2003).
- R. Agrawal, N. R. Singh, F. H. Ribeiro, W. N. Delgass, *Proc. Natl. Acad. Sci. U.S.A.* **104**, 4828 (2007).
- ICIS pricing report, www.icis.com/v2/chemicals/9075158/benzene/pricing.html.
- This work was supported by the U.S. Department of Energy Office of Energy Efficiency and Renewable Energy, under grant DE-FG36-08G018212; and by the Defense Advanced Research Projects Agency (DARPA) through the Defense Science Office Agreement HR0011-09-C-0075 (Approved for Public Release, Distribution Unlimited); the National Basic Research Program of China (973 Program, grant no. 2010CB732206); and the National Natural Science Foundation of China (grant no. 51076031). The views, opinions, and/or findings contained in this article/presentation are those of the author/presenter and should not be interpreted as representing the official views or policies, either expressed or implied, of the DARPA or the Department of Defense. We thank A. Javadi for the microfiltration of bio-oil, Y. Cheng for help with zeolite upgrading experiments, and the National Renewable Energy Laboratory and P. H. Steele from the Forest Products Department at Mississippi State University for providing us with bio-oil samples. The University of Massachusetts has filed a patent based on the methods presented here. G.W.H. has a financial interest in Anellotech, a privately held company focused on producing renewable petrochemicals from biomass.

Supporting Online Material

www.sciencemag.org/cgi/content/full/330/6008/1222/DC1
Materials and Methods
Figs. S1 and S2
Tables S1 to S8

24 June 2010; accepted 13 October 2010
10.1126/science.1194218

The Core Structure of Basal Dislocations in Deformed Sapphire (α -Al₂O₃)

A. H. Heuer,^{1*†} C. L. Jia,^{2*} K. P. D. Lagerlöf¹

The atomic structure of dislocation cores is decisive for the understanding of plasticity in crystalline solids. The core structure of dislocations in sapphire introduced by high-temperature plastic deformation has been investigated with the use of the negative spherical-aberration imaging technique. The ability of this technique to discriminate oxygen columns from aluminum (Al) columns, combined with reproduction of subtle contrast features by image simulation, leads to a markedly detailed atomic model of the dislocation cores. The partial dislocations are Al-terminated, with electrical neutrality being achieved because half of the Al columns are missing. These partials also undergo core spreading, which results in random occupancy of both tetrahedrally and octahedrally coordinated sites, though Al in tetrahedral coordination never occurs in a perfect crystal. Unusual dislocation core structures may be present in other technologically important nonmetallic solids.

Although ceramics are notorious for their brittle behavior under normal service conditions, plastic deformation in such materials can be realized at elevated temperatures, under circumstances in which friction and wear occur, and wherever cracking is suppressed by confining pressures, such as under an inden-

tation. Under all of these conditions, the behavior of dislocations, the principal “carrier” of plastic deformation in crystalline materials, assumes paramount importance.

Aluminum oxide (α -Al₂O₃) in both single-crystal form (sapphire) and as dense polycrystals finds utility in a wide range of important

applications, from laser hosts (Ti-sapphire) to inert ultrahard substrates. Plastic deformation at high temperatures by basal slip $\left((0001) \frac{1}{3} \langle 11\bar{2}0 \rangle \right)$ in sapphire ($\alpha\text{-Al}_2\text{O}_3$) was first reported by Wachtman and Maxwell in 1954 (1). Shortly thereafter, Kronberg (2) suggested that dissociation of basal dislocations into half partials could occur

$$\frac{1}{3} \langle 11\bar{2}0 \rangle \rightarrow \frac{1}{3} \langle 10\bar{1}0 \rangle + \frac{1}{3} \langle 01\bar{1}0 \rangle \quad (1)$$

with further dissociation into quarter partials also possible.

$$\frac{1}{3} \langle 10\bar{1}0 \rangle \rightarrow \frac{1}{9} \langle 2\bar{1}\bar{1}0 \rangle + \frac{1}{9} \langle 11\bar{2}0 \rangle \quad (2)$$

Equation 1 involves faulting only in the cation sublattice, as $\frac{1}{3} \langle 10\bar{1}0 \rangle$ is a translation vector of the anion sublattice. Nevertheless, the fault arising from reaction (1) on the basal plane has a very high

stacking fault energy (SFE), $\sim 1.5 \text{ J/m}^2$ (3), and such glide dissociation has never been observed. However, the $\frac{1}{3} \langle 10\bar{1}0 \rangle$ SFE is very anisotropic, and climb dissociation of basal dislocations at elevated temperatures is ubiquitous, due to the SFE being ~ 5 to 10 times smaller on the prism planes (4). Equation 2 involves an even higher SFE but may occur in the core of the $\frac{1}{3} \langle 01\bar{1}0 \rangle$ partials [core spreading (5)].

Figure 1A is a schematic representation of dislocation motion in sapphire. A 90° (edge) dislocation is shown gliding on a basal plane with a narrow stacking fault (width of $2b$, where b is the Burgers vector); this dislocation would appear undissociated if it could be imaged with a transmission electron microscope (6). The cores of the $\frac{1}{3} \langle 10\bar{1}0 \rangle$ partials have probably undergone core spreading, as suggested earlier (5), but again, this would not be discernable by conventional transmission electron microscopy (TEM). If a glissile dislocation were immobilized for any reason, the anisotropic SFE would lead to the configuration shown in Fig. 1A (iii), due to the much lower SFE for a $\frac{1}{3} \langle 10\bar{1}0 \rangle$ fault on $\{11\bar{2}0\}$ compared with (0001).

In proposing the importance of dislocation dissociation to the glide of basal dislocations in sapphire, Kronberg used an idealized version of

the structure of sapphire: a perfect hexagonal close-packed (hcp) oxygen sublattice and flat cation sheets. In reality, and as shown in supporting on-line material (SOM) fig. S1 (7), the oxygen sublattice is slightly distorted away from perfect hcp stacking, and the cation layers are “puckered.”

Although not discussed by Kronberg in his 1957 paper, this model of dislocation motion in sapphire required the motion plane to be between cation and anion layers and thus involves charge transport during dislocation motion. In spite of the fact that this must represent a substantial impediment to slip in a material with such strongly ionic bonding as $\alpha\text{-Al}_2\text{O}_3$, this aspect of dislocations in sapphire was ignored by Kronberg and the several other groups who subsequently studied deformation in $\alpha\text{-Al}_2\text{O}_3$ for the next four decades.

Using the actual, as opposed to the idealized, version of the crystal structure of sapphire, Bilde-Sørensen *et al.* (8) in 1996 presented a model for basal slip, again involving the $\frac{1}{3} \langle 10\bar{1}0 \rangle$ half partials of Eq. (1), but also a motion plane within the puckered cation layer. In this model, each $\frac{1}{3} \langle 10\bar{1}0 \rangle$ partial dislocation, as it moves to the half-slipped position, transports only half of the cations and, thus, does not involve any net charge transport, with the trailing partial restoring a

¹Department of Materials Science and Engineering, Case Western Reserve University, Cleveland, OH 44106, USA.

²Institute of Solid State Research and Ernst Ruska-Centre for Microscopy and Spectroscopy with Electrons (ER-C), Forschungszentrum Jülich GmbH, D-52425 Jülich, Germany.

*These authors contributed equally to this work.

†To whom correspondence should be addressed. E-mail: heuer@case.edu

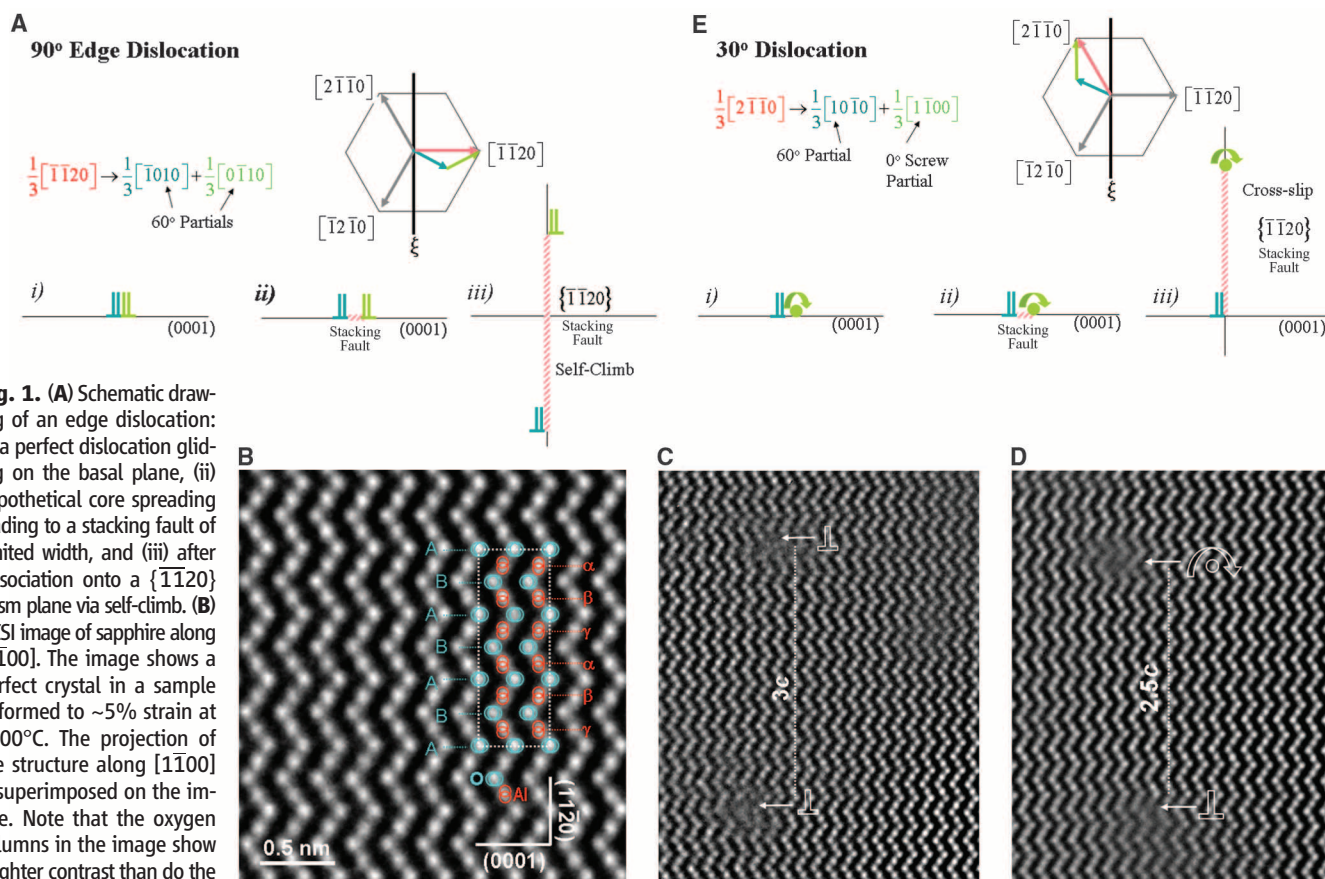


Fig. 1. (A) Schematic drawing of an edge dislocation: (i) a perfect dislocation gliding on the basal plane, (ii) hypothetical core spreading leading to a stacking fault of limited width, and (iii) after dissociation onto a $\{11\bar{2}0\}$ prism plane via self-climb. (B) NCSI image of sapphire along $[1100]$. The image shows a perfect crystal in a sample deformed to $\sim 5\%$ strain at 1400°C . The projection of the structure along $[1100]$ is superimposed on the image. Note that the oxygen columns in the image show brighter contrast than do the Al columns. (C) NCSI image of a climb-dissociated edge dislocation in the foil used for (B). Arrows indicate the cores of the partial dislocations. (D) NCSI image of a 30° dislocation. (E) Schematic drawing of a 30° mixed dislocation: (i) a perfect dislocation

gliding on the basal plane, (ii) hypothetical core spreading leading to a stacking fault of limited width, and (iii) after dissociation onto a $\{11\bar{2}0\}$ prism plane via cross-slip.

perfect lattice. Even though the SFE for basal slip is too large to allow resolvable glide dissociation (6), the Bilde-Sørensen *et al.* model describes the atomic motion within the dislocation core as the dislocation moves one Burgers vector.

Shibata *et al.* (9) used scanning TEM to study climb-dissociated basal dislocations within a small-angle bicrystal boundary in sapphire and concluded that the core structures of the dissociated dislocations were nonstoichiometric and therefore electrically charged. They further suggested that these charged, nonstoichiometric partials were characteristic of glissile basal dislocations that are active during high-temperature plastic deformation in α -Al₂O₃, and they developed a variant of Kronberg's synchroshear model to describe the motion of the nonstoichiometric partials. They did not consider the implications of charged dislocations on basal slip in sapphire.

Lagerlöf *et al.* (5) subsequently considered the implications of nonstoichiometric and charged dislocation cores on the motion of glide dislocations in a bulk sapphire crystal undergoing basal deformation at elevated temperatures and concluded that such nonstoichiometric dislocations cores are unlikely to be involved in high-temperature basal deformation. However, it may be possible for nonstoichiometric charged dislocation cores to exist in a periodic array in a manufactured small-angle boundary.

The purpose of the present work was to determine the core structure of basal dislocations in a sapphire single crystal deformed to ~5% strain at 1400°C with the use of the negative spherical-aberration imaging (NCSI) technique (10). In the image of a perfect crystal from such a specimen

shown in Fig. 1B, the projection of the sapphire structure along the [1 $\bar{1}$ 00] viewing direction is superimposed on the image, allowing identification of the atomic positions of both oxygen and Al columns. Along this viewing direction, the puckered Al cation layers are seen to consist of pairs of columns in the structure projection. In the image, the pairs of Al columns in the puckered layers cannot be resolved due to the resolution limit of the instrument (~80 pm).

An NCSI image of an edge dislocation that had dissociated by climb into two $\frac{1}{3}\langle 10\bar{1}0 \rangle$ partials is shown in Fig. 1C; these must be 60° partials. We have previously measured the SFE of climb-dissociated edge dislocations with conventional TEM (11) and found (from the separation of $\frac{1}{3}\langle 10\bar{1}0 \rangle$ partials) the SFE to be between 0.1 and 0.25 J/m²; the image in Fig. 1C (assuming the partials are at a friction-free equilibrium) suggests a SFE of 0.21 J/m² (12).

Other dislocations in this TEM foil appeared with a single $\frac{1}{3}\langle 10\bar{1}0 \rangle$ partial visible (Fig. 1D). The second partial must have either a Burgers vector parallel to the viewing direction ($\frac{1}{3}\langle 10\bar{1}0 \rangle$) or pure screw character, as such an image would not be possible for a pure edge dislocation. Given the edge component visible at the bottom of the image, this dislocation must be a 60° $\frac{1}{3}\langle 10\bar{1}0 \rangle$ partial. At a distance of 2.5c (where c is the unit cell parameter along <0001>) above the $\frac{1}{3}\langle 10\bar{1}0 \rangle$ partial, faint contrast is evident, similar to that of the dislocation core in Fig. 1C. However, there is no edge component of the Burgers vector at this position. We believe that the dislocation imaged in Fig. 1D is a 30° dislocation that had dissociated to a 60° partial and a screw partial; the config-

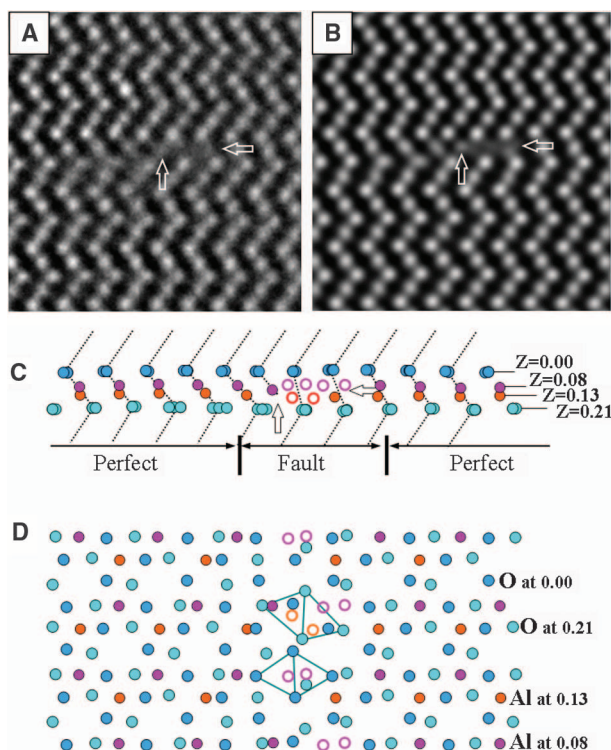
uration imaged in this figure probably formed by cross slip after the 30° glissile dislocation had been immobilized (Fig. 1E). The separation of the two partials suggests a SFE of 0.17 J/m² (13).

We focused on these 60° $\frac{1}{3}\langle 10\bar{1}0 \rangle$ partials for determining the dislocation core structure at atomic resolution; in particular, the images of such 60° partials contained a similar set of contrast features (see fig. S2). These include (i) modest contrast of the terminating Al columns in comparison with the equivalent columns on the left-hand side of the dislocations; (ii) strongly reduced contrast of the Al columns on the right-hand side of the terminating columns, in comparison with the equivalent columns in areas of perfect lattice, as denoted by the lateral arrows; and (iii) similar image contrast of the oxygen columns at the cores compared with that in perfect crystal.

The common image-contrast features at the dislocation cores have been successfully reproduced by means of quantum-mechanical and optical image simulation (14). As a representative example, the experimental image of Fig. 2A has been selected for direct comparison with image simulation. A trial defect structure is assumed, and images are calculated by solving the Schrödinger equation for the electron wave function, taking into account effects of specimen thickness and crystal tilt. The image intensity distribution is calculated, also considering the effects of residual lens aberrations. By the use of an established comparison procedure (15), the atomic structure model is modified in an iterative manner until an optimum fit to the experimental image-contrast distribution is obtained (Fig. 2B). Furthermore, surface relaxation around a dislocation intersecting a free surface, the so-called Eshelby twist (16–19), is possible in a TEM foil because of the shear stresses associated with the screw component of the dislocation. This effect has been included in the simulation.

The atomic positions at the dislocation core are displayed in a [1 $\bar{1}$ 00] projection in Fig. 2C and in a basal plane projection in Fig. 2D; the core extends over four atomic planes. For clarity, three (0001) atomic layers, including the dislocation core and involving the puckered Al layer sandwiched between two oxygen layers, are shown in Fig. 2C. The displacements due to the extra half plane of the partial dislocation are confined to the two lattice planes on either side of the partial dislocation; a number of Al atomic columns—those shown as open circles—have 50% occupancy of the Al cations with respect to a perfect lattice. Some of the Al cations are in tetrahedral coordination in the dislocation core, and the Al cations are randomly distributed between sites with tetrahedral and octahedral coordination. The model of the core structure clearly shows that the low contrast of the terminating Al column at the dislocation core is caused by the absence of half of a column pair. The reduced contrast of the Al columns on the right-hand side of the terminating Al column arises from relative displacement of the Al atoms away from the regular column positions.

Fig. 2. Experimental (A) and simulated (B) images of a 60° partial dislocation in deformed sapphire. The simulated image is calculated for a sample thickness of 4.1 nm, defocus = 5 nm, two-fold astigmatism = 2 nm, three-fold astigmatism = 30 nm, coma = 30 nm, crystal tilt of 2.0 mrad, and vibration of 0.03 nm. The simulation is based on a structure model with Eshelby twist. The details of the dislocation core are shown in the [1 $\bar{1}$ 00] projection in (C) and in a basal projection in (D). Open circles denote 50% occupancy. Vertical arrows indicate the modest contrast of the terminating Al column; horizontal arrows indicate the strongly reduced contrast of the Al columns on the right-hand side of the terminating column. Z denotes relative positions in nanometers.



On the basis of the satisfactory fit of the structure model to the experimental image, we suggest that the dislocation cores are neither charged nor nonstoichiometric. We note, however, that small changes in contrast occur at the individual dislocation cores in these 60° partials, which must reflect the randomness of the Al atoms in tetrahedral and octahedral coordination near the dislocation core (see fig. S2). In turn, these changes must depend on details of the associated local strain and lattice distortion.

The notion of Al^{3+} in tetrahedral coordination at a dislocation core was first suggested by Lagerlöf *et al.* (5) in a discussion of core spreading of a partial dislocation. They assumed that Eq. 2 occurred in the core of the $\frac{1}{3}\langle 10\bar{1}0 \rangle$ partials

and argued that steric constraints were sufficiently modest that such core spreading was likely. Figure 2 provides good evidence that their speculation was correct.

Assuming that the core structure portrayed in Fig. 2 is correct, we can now provide plausible atomistic models for glissile edge and 30° dislocations in sapphire. Consider an edge dislocation formed by the removal of two planes of atoms (as shown in Fig. 3, A and B) viewed along $[1\bar{1}00]$ and $[000\bar{1}]$, respectively, or the similarly formed 30° dislocation (shown in Fig. 3, C and D) (20). (Perfect crystal in these orientations is shown in fig. S1, B and C.) The terminating plane of Al^{3+} ions shows only 50% occupancy, and the spreading of the cores of the $\frac{1}{3}\langle 10\bar{1}0 \rangle$ partials results in

tetrahedral coordination of the Al^{3+} cations (compare with Fig. 2).

The structure models in Fig. 3 make clear that the relative displacements present in the dislocated crystal occur in the puckered Al layer (that is, between the two halves of the column pairs), consistent with the Bilde-Sørensen *et al.* model (8). The puckered Al layer consists of upper and lower sublayers of Al cations parallel to (0001) . The upper half layer is strongly bonded to the oxygen layer above it and the lower half layer to the oxygen layer below it. Because of the shear stress introduced by the dislocation, insertion or removal of half of an atomic plane causes a relative displacement between the two parts above and below the center of the dis-

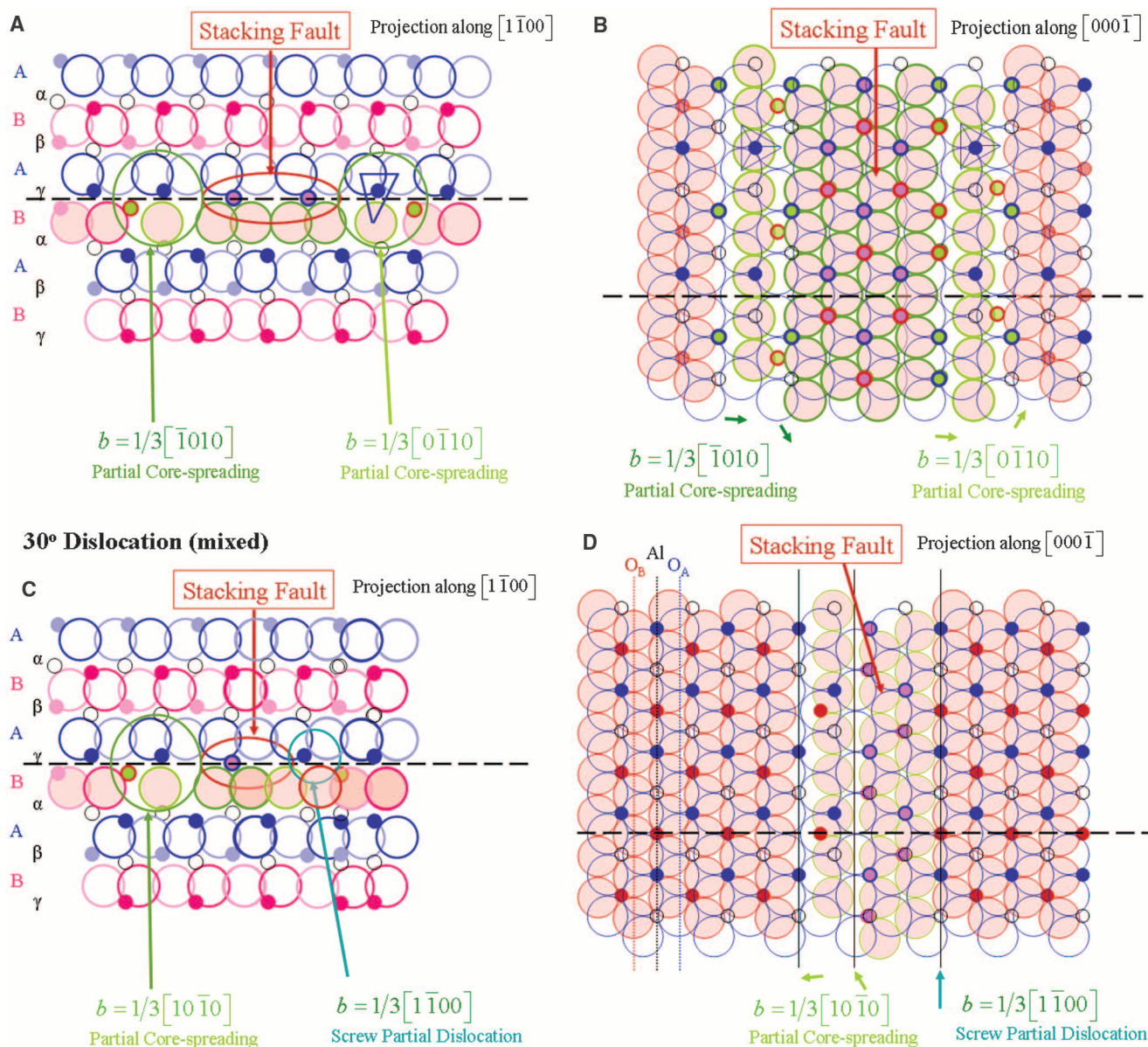


Fig. 3. Schematic representations of the structure of Al_2O_3 viewed along $[1\bar{1}00]$ (A) and (C) and also along $[000\bar{1}]$ (B) and (D), after removal of two planes of atoms. (A) and (B) show an edge partial, whereas (C) and (D) show a 30° partial. Note that a stacking fault of width $2b$ is assumed,

as is spreading of the cores of the $\frac{1}{3}\langle 10\bar{1}0 \rangle$ partials. The small open circles are normally empty octahedral interstitial sites. The triangles in (A) and (B) denote Al in tetrahedral coordination. O_A and O_B denote oxygen atoms in alternating layers.

location core, which occurs in the plane with relatively weak bonding (that is, between the upper and lower layers of the puckered Al layer). As no charge transport is involved, the Peierls barriers are smaller than if the dislocations were charged.

It is not clear whether the core structure of glissile basal dislocations shown in Fig. 3 should be expected for dislocations present in a low-angle boundary (9). The periodic electrostatic and stress fields present in such a boundary could well lead to a different core structure for its constituent dislocations.

The NCSI studies have also revealed a stacking fault on the basal plane (fig. S4), but only in the thinnest regions of the TEM foils; such faults have not been reported for α -Al₂O₃ as yet. Partial dislocations are present at the ends of the three distinct faults in this image. At the dislocation cores, similar contrast to that of the dislocation core in Fig. 2A is observed: Low contrast occurs in the puckered Al layer. The details of the contrast feature of the experimental image have been reproduced in the calculated image, indicating a rearrangement of the Al atoms in the puckered layer (fig. S5) (7).

The NCSI technique has been used to image, at atomic resolution, partial dislocations bounding prism-plane stacking faults in sapphire deformed at high temperatures. The dislocations appear to be stoichiometric and uncharged, and the cores exhibit 50% occupancy of the Al cations to achieve electrical neutrality. Because of core spreading, the Al ions at the termination of the extra half planes exhibit random occupancy of

sites showing tetrahedral and octahedral coordination. It is likely that the motion plane is within the puckered Al sublattice, following the Bilde-Sørensen *et al.* model (8) for gliding basal dislocations.

References and Notes

1. J. B. Wachtman Jr., I. H. Maxwell, *J. Am. Ceram. Soc.* **37**, 291 (1954).
2. M. L. Kronberg, *Acta Metall.* **5**, 507 (1957).
3. A. G. Marinopoulos, C. Elsässer, *Philos. Mag. Lett.* **81**, 329 (2001).
4. M. H. Jhon, A. M. Glaeser, D. C. Chrzan, *Phys. Rev. B* **71**, 214101 (2005).
5. K. P. D. Lagerlöf, J. Castaing, A. H. Heuer, *Philos. Mag.* **89**, 489 (2009).
6. Actually, the conventional concept of a well-defined stacking fault with a well-defined SFE may break down when the energy is as high as it is for sapphire on the basal plane. The configuration in Fig. 1A (ii) should be thought of as an extended core.
7. Supporting material is available on Science Online.
8. J. B. Bilde-Sørensen *et al.*, *Acta Mater.* **44**, 2145 (1996).
9. N. Shibata *et al.*, *Science* **316**, 82 (2007).
10. C. L. Jia, M. Lentzen, K. Urban, *Science* **299**, 870 (2003).
11. K. P. D. Lagerlöf *et al.*, *Acta Metall.* **32**, 97 (1984).
12. Theoretical density functional theory calculations (4) yielded (0 K) values of 0.42 or 0.35 J/m², depending on the computational scheme that was employed (local density approximation or generalized gradient approximation). This difference from the experimental value might be due to the neglect of temperature effects in the calculations. Shell-model calculations (4) of SFEs indicate reductions of 0.1 to 0.2 J/m² between 0 and 1800 K due to vibrational entropy effects.
13. The small difference between the SFE calculated from the separation of the dissociated edge and 30° partials is possibly due to the partials not having reached their equilibrium separation.

14. D. B. Williams, C. B. Carter, *Transmission Electron Microscopy* (Springer, Berlin, ed. 2, 2009).
15. C. L. Jia *et al.*, *Nat. Mater.* **7**, 57 (2008).
16. J. D. Eshelby, A. N. Stroh, *Philos. Mag.* **42**, 1401 (1951).
17. As discussed in the SOM (fig. S3), the simulations of the dislocation core structure with and without consideration of the Eshelby twist (fig. S3, B and C) are indistinguishable. This arises because of the very small displacements involved in the Eshelby twist (which displacements are not included in Fig. 2, C and D, but were included in Fig. 2B to allow comparison with the experimental image).
18. Although α -Al₂O₃ has a trigonal crystal structure (space group no. 167: $R\bar{3}c$, where R is the rhombohedral space lattice), it is remarkably isotropic elastically [the anisotropy factor is approximately $A = 0.857$ [see, for example, (19)]]. Hence, the Eshelby-Stroh formula, which applies to elastic isotropic solids, can be used to a first approximation.
19. D. S. Phillips, T. E. Mitchell, A. H. Heuer, *Philos. Mag. A* **45**, 1371 (1982).
20. Note that the dislocations are again portrayed to have dissociated to a width of $\sim 2b$, and the cores of both partials have undergone core spreading.
21. We are grateful to L. Houben (ER-C, Jülich, Germany) for his help in modeling the Eshelby twist for the 60° partial dislocation and to K. Urban (ER-C, Jülich, Germany), M. Rühle (Max Planck Institute for Metals Research, Stuttgart, Germany), F. Ernst [Case Western Reserve Univ. (CWRU), Cleveland, OH], and P. Pirouz (CWRU, Cleveland, OH) for useful discussions.

Supporting Online Material

www.sciencemag.org/cgi/content/full/330/6008/1227/DC1

SOM Text

Figs. S1 to S5

References

14 May 2010; accepted 27 October 2010
10.1126/science.1192319

How Cats Lap: Water Uptake by *Felis catus*

Pedro M. Reis,^{1,2*} Sunghwan Jung,^{3*} Jeffrey M. Aristoff,^{4*} Roman Stocker^{1*†}

Animals have developed a range of drinking strategies depending on physiological and environmental constraints. Vertebrates with incomplete cheeks use their tongue to drink; the most common example is the lapping of cats and dogs. We show that the domestic cat (*Felis catus*) laps by a subtle mechanism based on water adhesion to the dorsal side of the tongue. A combined experimental and theoretical analysis reveals that *Felis catus* exploits fluid inertia to defeat gravity and pull liquid into the mouth. This competition between inertia and gravity sets the lapping frequency and yields a prediction for the dependence of frequency on animal mass. Measurements of lapping frequency across the family Felidae support this prediction, which suggests that the lapping mechanism is conserved among felines.

Terrestrial animals have evolved diverse means to acquire water, including absorption through the skin (1) or extraction of moisture from food (2), but most rely on drinking (3–12). Drinking presents a challenge to land vertebrates, because fresh water occurs mainly as horizontal liquid surfaces, such as puddles, ponds, lakes, or streams, and animals must displace water upward against gravity to drink it. Crucial in the drinking process is the role of the tongue, which in vertebrates is used in two distinctly different ways. Vertebrates with complete cheeks, such as pigs,

sheep, and horses, use suction to draw liquid upward and use their tongue to transport it intraorally (13, 14). In contrast, vertebrates with incomplete cheeks, including most carnivores, are unable (after weaning) to seal their mouth cavity to generate suction and must rely on their tongue to move water into the mouth (13). When the tongue sweeps the bottom of a shallow puddle, the process is called licking (4). When the puddle is deeper than the tongue excursion into the liquid, it is called lapping (15). Here, we report on the lapping mechanism of the domestic cat (*Felis catus*).

Almost everyone has observed a domestic cat lap milk or water. Yet casual observation hardly captures the elegance and complexity of this act, as the tongue's motion is too fast to be resolved by the naked eye. We used high-speed imaging to capture the motion of both the tongue and liquid during lapping [Fig. 1 and movie S1 (16)]. With the cat's face oriented downward, the tongue extends from the jaw (Fig. 1A) and its tip curls sharply caudally (Fig. 1B). At the lowest position of the tongue's tip, its dorsal side rests on the liquid surface, without piercing it (Fig. 1B). When the cat lifts the tongue, liquid adhering to the dorsal side of the tip is drawn upward, forming a column (Fig. 1C). This liquid column is further extended by the tongue's upward motion (Fig. 1D), thinning in the process (Fig. 1E), and is finally partially captured upon jaw closure (Fig. 1, E and F). Inside the mouth, cavities

¹Department of Civil and Environmental Engineering, Massachusetts Institute of Technology (MIT), Cambridge, MA 02139, USA. ²Department of Mechanical Engineering, MIT, Cambridge, MA 02139, USA. ³Department of Engineering Science and Mechanics, Virginia Polytechnic Institute and State University, Blacksburg, VA 24061, USA. ⁴Department of Mechanical and Aerospace Engineering, Princeton University, Princeton, NJ 08544, USA.

*All authors contributed equally to this work.

†To whom correspondence should be addressed. E-mail: romans@mit.edu